Heat treatment protocol for modulating ionic conductivity via structural evolution of $Li_{3-x}Yb_{1-x}M_xCl_6$ (M = Hf^{4+}, Zr^{4+}) new halide superionic conductors for all-solid-state batteries

Juhyoun Park [a,c,1], Daseul Han [b,1], Hiram Kwak [a,c], Yoonjae Han [a,c], Yong Jeong Choi [b], Kyung-Wan Nam [b,*], Yoon Seok Jung [a,*]

[a] *Department of Chemical and Biomolecular Engineering, Yonsei University, Seoul 03722, South Korea*
[b] *Department of Energy and Materials Engineering, Dongguk University, Seoul 04620, South Korea*
[c] *Department of Energy Engineering, Hanyang University, Seoul 04763, South Korea*

ARTICLE INFO

ABSTRACT

Owing to their deformability and good (electro)chemical-oxidation stability, halide superionic conductors have emerged as enablers for practical all-solid-state batteries. Herein, we report the dynamic structural evolution of Li_3YbCl_6, which varies with the heat treatment temperature (400 vs. 500 °C) and aliovalent substitutions with Hf^{4+} or Zr^{4+}. It is observed that slight differences in Li^+ conductivities (0.19 vs. 0.14 mS cm^{-1} at 30 °C) and activation energies (0.47 vs. 0.53 eV) between unsubstituted Li_3YbCl_6 heat-treated at 400 and 500 °C diverge upon aliovalent substitution, which results in the evolution of monoclinic and orthorhombic phases, respectively. Enhanced Li^+ conductivities reaching 1.5 mS cm^{-1} with an activation energy of 0.26 eV ($Li_{2.60}Yb_{0.60}Hf_{0.40}Cl_6$ prepared at 400 °C) upon Hf^{4+}- or Zr^{4+}-substitution are ascribed to the optimal concentration of charge carriers of Li^+ and vacancies. Importantly, the exclusive comparison of crystal structures affecting Li^+ conductivity in halide superionic conductors is enabled for the first time, demonstrating that it is more favorable for the cubic close-packed (ccp) monoclinic structure as compared to the hexagonal close-packed (hcp) orthorhombic structure. Furthermore, the excellent reversibility of single-crystalline $LiNi_{0.88}Co_{0.11}Al_{0.01}O_2$ in all-solid-state cells at 30 °C was achieved by employing ccp monoclinic $Li_{2.60}Yb_{0.60}Hf_{0.40}Cl_6$ prepared at 400 °C with a capacity retention of 83.6% after 1000 cycles.

1. Introduction

Lithium-ion battery (LIB) technology has revolutionized the electrification of transportation [1,2]. However, a breakthrough in terms of improved safety and energy density is necessary, which could be enabled by solidifying electrolytes with non-flammable inorganic superionic conductors [3–10]. Development of novel solid electrolytes (SEs) that can meet multiple requirements (i.e., high ionic conductivity, mechanical sinterability, and (electro)chemical stability) is thus the key to practical all-solid-state Li batteries (ASLBs) [3–10].

Among SEs, oxide SE families are one of the most extensively investigated candidates [11–15]. Despite their Li^+ conductivities of 10^{-4}–10^{-3} S cm^{-1}, moderate chemical stabilities in ambient air, and good electrochemical stabilities, their integration into bulk-type ASLBs

requires either a detrimental high-temperature sintering process or hybridization with polymer electrolytes [14–20]. Sulfide SE materials are mechanically sinterable and highly conductive (maximum conductivities of ~ 10^{-2} S cm^{-1}) [4–6,8,21–26]. Unfortunately, their (electro) chemical instabilities are critical limitations [6,23,27,28]. Sulfide SEs release toxic H_2S gases upon exposure to ambient air [6,23,27]. In addition, their intrinsic electrochemical oxidation stability limits are in the range of 2–3 V (vs. Li/Li^+) [6,28]. Specifically, uncoated layered $LiMO_2$ cathode materials paired with sulfide SEs exhibited poor electrochemical performances due to their large interfacial resistances [29–31]. Borohydride SE materials are another class of superionic conductors that exhibit mechanical sinterability [32,33]. Nevertheless, complicated synthetic protocols and/or extremely expensive precursors and limited anodic stabilities remain to be resolved for practical

applications.

Recently, emerging halide SEs are unique in that they simultaneously satisfy the requirements of both excellent (electro)chemical oxidation stability and deformability [34–42]. Trigonal Li_3MCl_6 (M = Y, Er, ~0.51 mS cm^{-1}) is the first halide SE material that has been investigated [34]. Its trigonal structure (space group: $P\bar{3}m1$) is based on a hexagonal closed-packed (hcp) anionic framework, where the Li^+ ions, metal ions, and vacancies occupy octahedral sites, exhibiting 3D Li^+ diffusion pathways with favorable 1D paths along the c-axis via face-shared octahedra (Fig. 1a, b) [36,37,39]. Exploration of a new composition based on Li_3MCl_6 (M = Y, Er) led to the identification of several halide superionic conductors including monoclinic Li_3InCl_6 (~2 mS cm^{-1}) [35], orthorhombic $Li_{3-x}M_{1-x}Zr_xCl_6$ (M = Y, Er, max. ~ 1.4 mS cm^{-1}) [37], spinel $Li_2Sc_{2/3}Cl_4$ (1.5 mS cm^{-1}) [40], monoclinic Li_xScCl_{3+x} (max. 3 mS cm^{-1}) [38], and trigonal Fe^{3+}-substituted Li_2ZrCl_6 (max. ~ 1 mS cm^{-1}) [41]. Specifically, the aliovalent substitution of Li_3MCl_6 (M = Y, Er) with Zr^{4+} led to a structural transition from a trigonal structure,

through a previously known orthorhombic structure (*Pnma*, Fig. 1c, d, denoted as "orthorhombic I") [43], to the new orthorhombic structure (*Pnma*, Fig. 1e, f, denoted as "orthorhombic II") [37].

The Li^+ conductivities of these halide SEs varied significantly due to multiple factors, such as crystal structure and synthetic protocol, which has been a highly intriguing topic [37–39,44,45]. The much higher Li^+ conductivity of mechanochemically prepared Li_3MCl_6 (M = Y, Er) compared to the high-crystalline annealed samples was explained by M site disordering, which broadens Li^+ diffusion channels [44]. Besides, it was suggested that the high ionic conductivity of Li_3InCl_6 could be attributed to 3D Li^+ diffusion channels in the cubic closed-packed (ccp) monoclinic structure, where Li^+ channels are formed via octahedral-tetrahedral-octahedral sites (*C2/m*, Fig. 1g, h) [36,37,39]. However, monoclinic Li_2ZrCl_6 prepared at 260 °C exhibited a poor Li^+ conductivity of 5.7×10^{-6} S cm^{-1}, which was in sharp contrast to that of the mechano-chemically-derived trigonal phase of the same composition (4×10^{-4} S cm^{-1}) [41]. This instance reflects the complicated factors
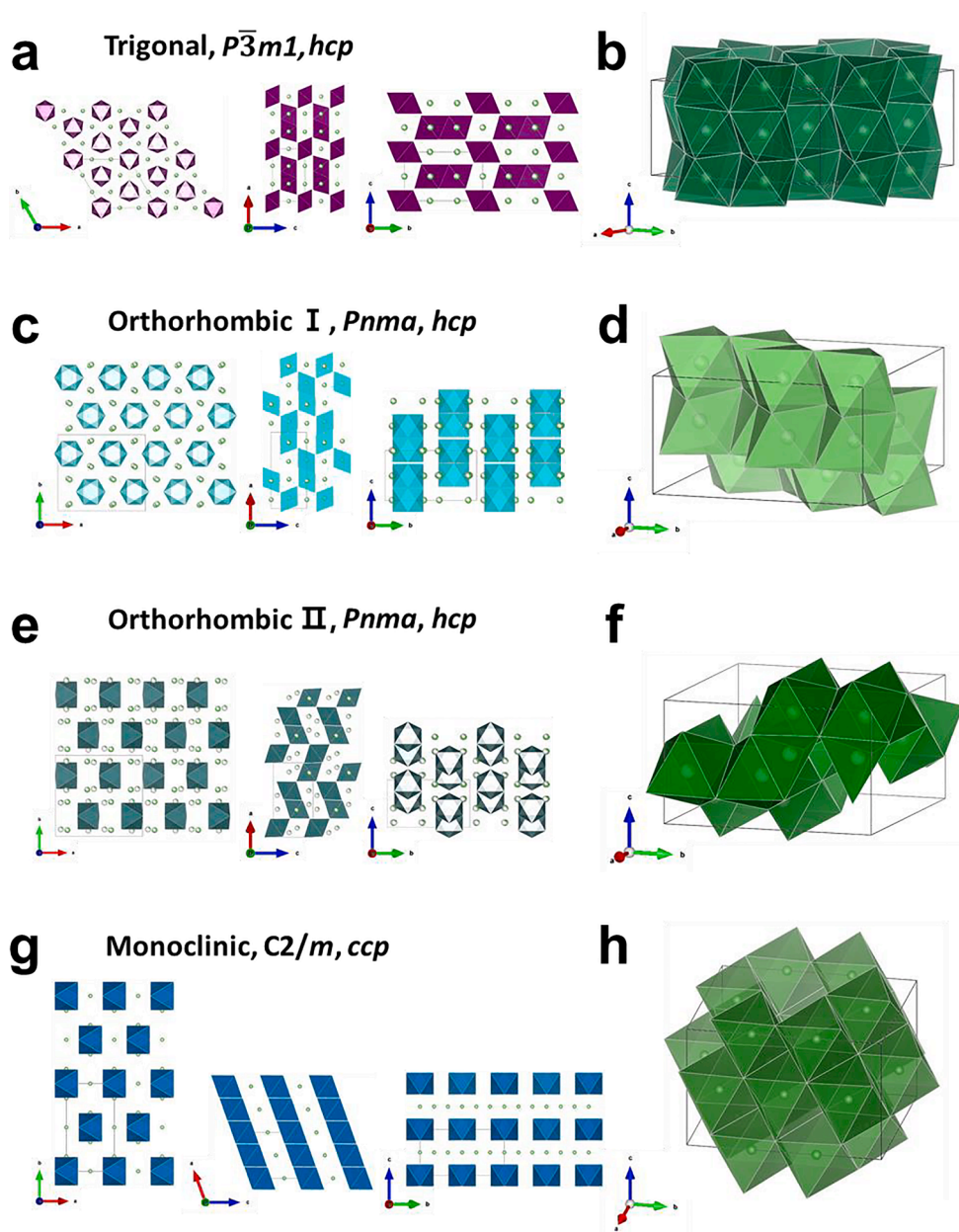

Fig. 1. Crystal structures outlined with the unit cells and corresponding Li^+ substructures of (a, b) trigonal Li_3MCl_6 (M = Y, Tb-Tm), (c, d) orthorhombic I Li_3MCl_6 (M = Yb, Lu), (e, f) orthorhombic II $Li_{2.5}M_{0.5}Zr_{0.5}Cl_6$ (M = Y, Er), and (g, h) monoclinic Li_3InCl_6.

affecting Li$^+$ migration in halide SEs. It has been proposed that inter-coupled multiple factors, including anionic lattice structure [36,37], M site disordering [44], Li contents [38,45], tetrahedral Li occupation [45,46], and concentration and distribution of metal ions [45], could affect Li$^+$ migration in halide SE materials. Specifically, most halide superionic conductors identified thus far possess either hcp or ccp structures. It was inferred or theoretically suggested that the ccp structure is more advantageous for Li$^+$ migration in halide SEs, while direct experimental verification is yet to be demonstrated [37,39].

The crystal structure of Li-M-Cl compounds seems to be determined by the ionic radius of M^{n+} ions (a mean value of ionic radii for the presence of multiple metals) [37,39,43]. In 1997, Meyer and coworkers suggested that the crystal structure of Li$_3$MCl$_6$ is changed by decreasing the ionic radius of M^{3+} (Er, Yb, Sc) from trigonal, through orthorhombic I, to monoclinic [43], which is in accordance with the recently investigated series of substituted compounds of Li$_3$Y$_{1-x}$In$_x$Cl$_6$ and Li$_{3-x}$M$_{1-x}$Zr$_x$Cl$_6$ (M = Y, Er) [37,39].

While Li$_3$YbCl$_6$ was known to have an orthorhombic I structure [43], interestingly, we have found that it crystallizes differently and shows slightly different Li$^+$ conductivities and activation energies via heat treatment (HT) at different temperatures: trigonal (0.19 mS cm^{-1} and 0.47 eV) and orthorhombic I (0.14 mS cm^{-1} and 0.53 eV) phases when heat-treated at 400 and 500 °C, respectively. Thus, Li$_3$YbCl$_6$ provides a good model system to deconvolute the effect of the crystal structure on Li$^+$ conductivity. Furthermore, it is shown that the aliovalent substitution of Yb^{3+} with tetravalent metal ions of Hf^{4+} and Zr^{4+} leads to drastic phase transitions to monoclinic and orthorhombic II, respectively, and boosting of Li$^+$ conductivity, which reaches 1.5 mS cm^{-1} with an activation energy of 0.26 eV (Li$_{2.60}$Yb$_{0.60}$Hf$_{0.40}$Cl$_6$). Importantly, the distinctly different phase transitions between samples heat-treated at 400 and 500 °C led to more divergent Li$^+$ conductivities and activation energies. The excellent cycling performance of single-crystalline LiNi$_{0.88}$Co$_{0.10}$Al$_{0.02}$O$_2$ (single-NCA88) employing Li$_{2.60}$Yb$_{0.60}$Hf$_{0.40}$Cl$_6$ and Li$_{2.80}$Yb$_{0.80}$Zr$_{0.20}$Cl$_6$ prepared at 400 °C was also demonstrated.

2. Results and discussion

Li$_{3-x}$Yb$_{1-x}$M$_x$Cl$_6$ (M = Hf, Zr) samples were synthesized by mechanochemical milling of stoichiometric amounts of LiCl, HfCl$_4$ or ZrCl$_4$, and YbCl$_3$ precursors, followed by HT at 400 or 500 °C for 6 h. The high-resolution X-ray diffraction (HRXRD) patterns using synchrotron radiation and the Rietveld refinement profiles for Li$_3$YbCl$_6$ heat-treated at 400 and 500 °C are presented in Fig. 2a. The refined crystallographic parameters are listed in Tables S1 and S2. Intriguingly, Li$_3$YbCl$_6$ prepared at 400 °C was crystallized to the hcp trigonal structure like Li$_3$MCl$_6$ (M = Y, Er) [34,43], while the sample prepared at 500 °C formed the original orthorhombic I structure [43]. These results indicate that the formation energy of the orthorhombic I phase is slightly more negative than that of the trigonal structure. The Li$^+$ conductivities of Li$_3$YbCl$_6$ were measured by the AC impedance method using Ti/SE/Ti symmetric Li$^+$ blocking cells. Arrhenius plots of the Li$^+$ conductivities and the corresponding activation energies are shown in Fig. 2b. Notably, the activation energy of Li$_3$YbCl$_6$ prepared at 400 °C with a trigonal structure (0.47 eV) was lower than that prepared at 500 °C with an orthorhombic I structure (0.53 eV). In addition, the Li$^+$ conductivity of Li$_3$YbCl$_6$ was slightly higher when heat-treated at 400 °C (0.19 mS cm^{-1}), compared to the one heat-treated at 500 °C (0.14 mS cm^{-1}). The Rietveld refinement results show that the trigonal Li$_3$YbCl$_6$ prepared at 400 °C had a 3.6% M2-M3 site disorder (M2 and M3 sites have the same x and y but different z position in the lattice, Tables S1) and a slightly smaller lattice size (645.100 Å^3) in comparison with that of Li$_3$YCl$_6$ (655.723 Å^3) or Li$_3$ErCl$_6$ (660.350 Å^3) (Tables S1), which is rationalized by the highly crystalline features of the heat-treated sample and the smaller ionic radius of Yb^{3+} (87 pm) vs. Y^{3+} (90 pm) or Er^{3+} (89 pm), respectively [44].

A control experiment was also carried out using Li$_{2.5}$Y$_{0.5}$Zr$_{0.5}$Cl$_6$, which crystallizes from a trigonal to orthorhombic II structure upon increasing the HT temperature (Fig. S1) [37]. While Li$_{2.5}$Y$_{0.5}$Zr$_{0.5}$Cl$_6$ prepared at 200 °C showed a trigonal structure, the orthorhombic II phase started to evolve with increasing HT temperatures. Accordingly, slightly decreased Li$^+$ conductivities and increased activation energies were obtained. This result may also support the more favorable structure of the trigonal phase over the orthorhombic II phase. However, M site disordering effects that render the Li$^+$ substructure cannot be excluded [44].

To enhance the Li$^+$ conductivity of Li$_3$YbCl$_6$, aliovalent substitution with Hf^{4+} was attempted for the heat-treated samples at 400 or 500 °C. The XRD patterns and Li$^+$ conductivities with the corresponding activation energies are shown in Fig. 3. When Li$_{3-x}$Yb$_{1-x}$Hf$_x$Cl$_6$ was prepared at 400 °C (Fig. 3a), a trigonal structure was preserved up to x = 0.10. However, further substitution of x > 0.10 resulted in a drastic phase transition. The evolution of the monoclinic phase observed for Li$_3$InCl$_6$ [35] started to evolve at x = 0.25. For 0.40 ≤ x ≤ 0.60, the main reflections in the XRD patterns belong to the monoclinic phase. The minor phase was indexed as the orthorhombic II phase, which was observed when Li$_{3-x}$Yb$_{1-x}$Hf$_x$Cl$_6$ was prepared at 500 °C (x ≥ 0.25, Fig. 3b). At x =
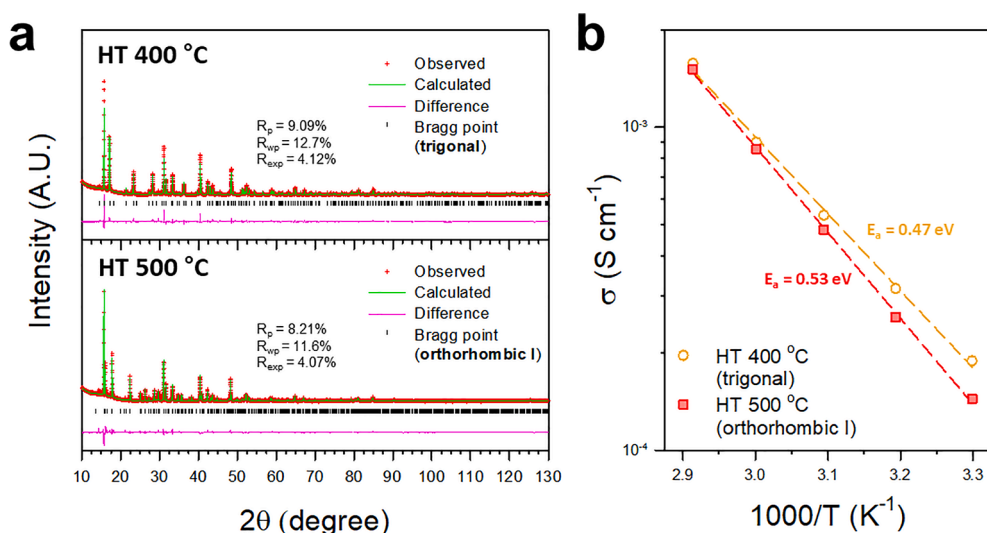

Fig. 2. Observed and calculated high-resolution synchrotron radiation X-ray Rietveld refinement profiles and (b) Arrhenius plots of Li$^+$ conductivity for Li$_3$YbCl$_6$ heat-treated at 400 or 500 °C for 6 h. Rietveld refinement results are shown in Tables S1 and S2.
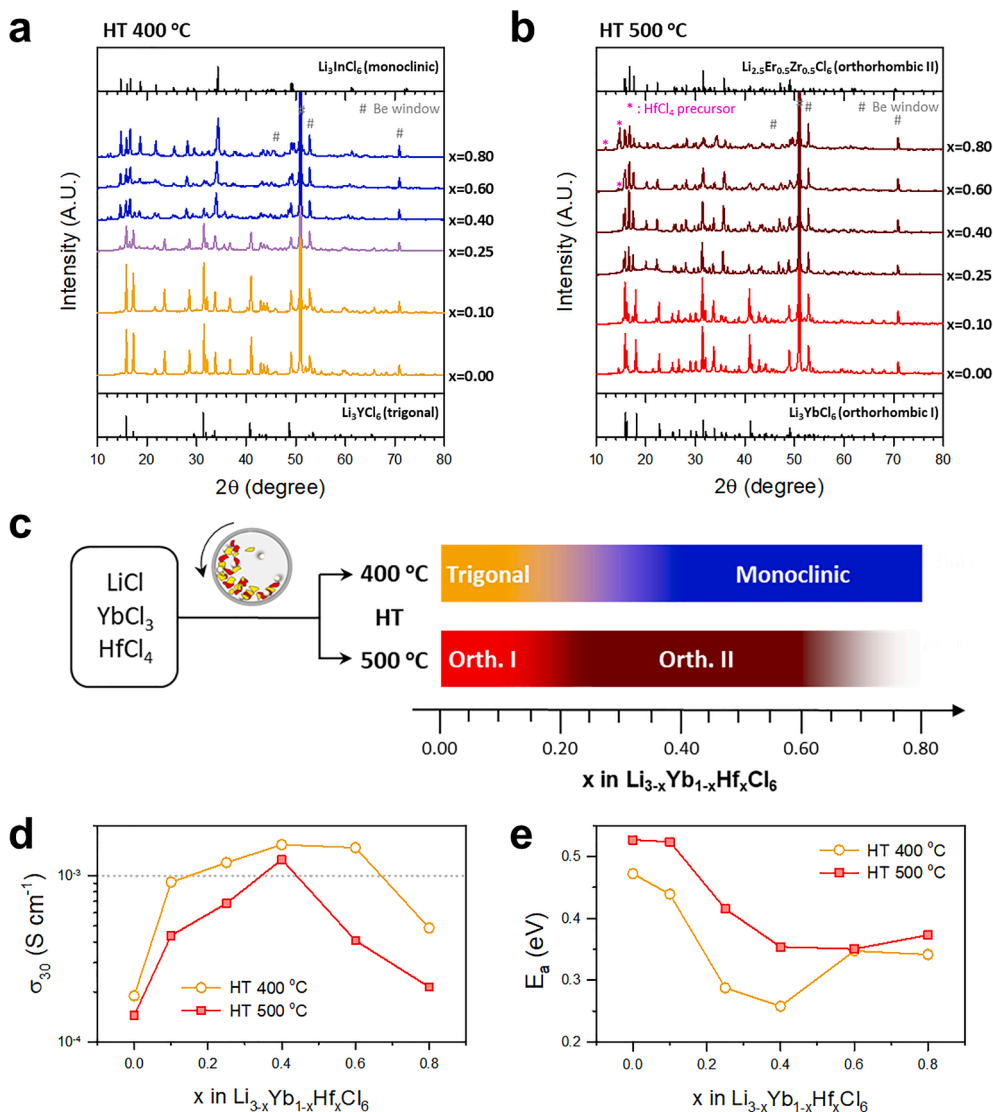
Fig. 3. Results of structural evolution and corresponding Li^+ conductivities with activation energies for Hf^{4+}-substituted Li_3YbCl_6 annealed at 400 and 500 °C for 6 h. XRD patterns of $Li_{3-x}Yb_{1-x}Hf_xCl_6$ annealed at (a) 400 °C and (b) 500 °C. (c) Schematic illustrating the phase evolutions upon Hf^{4+}-substitution of Li_3YbCl_6 prepared at 400 or 500 °C. (d) Li^+ conductivities at 30 °C and (e) corresponding activation energies for $Li_{3-x}Yb_{1-x}Hf_xCl_6$.

0.80, a high-purity monoclinic phase was obtained. For $Li_{3-x}Yb_{1-x}Hf_xCl_6$ prepared at 500 °C, the orthorhombic I structure was maintained at x ≤ 0.10. More substitution (x ≥ 0.25) resulted in the orthorhombic II structure, which is isostructural with the orthorhombic phase of $Li_{3-x}M_{1-x}Zr_xCl_6$ (M = Y, Er, 0.367 < x < 0.6) [37]. At x = 0.80, the signatures of the $HfCl_4$ precursor was detected at the expense of the reflections for the orthorhombic II phase, indicating the solid-solution limit of x < 0.80. A summary of the afore-described phase evolutions upon Hf^{4+}-substitution for Li_3YbCl_6 prepared at 400 or 500 °C is displayed in Fig. 3c.

Fig. 3d, e displays Li^+ conductivities and corresponding activation energies, respectively, for $Li_{3-x}Yb_{1-x}Hf_xCl_6$ (0.0 ≤ x ≤ 0.8) prepared at 400 or 500 °C. Typical Nyquist plots at different temperatures and corresponding Arrhenius plots of Li^+ conductivity are also presented in Fig. S2. Low electronic conductivity of $Li_{3-x}Yb_{1-x}Hf_xCl_6$ was measured (4.5×10^{-9} S cm^{-1} for $Li_{2.60}Yb_{0.60}Hf_{0.40}Cl_6$ prepared at 400 °C, Fig. S3), confirming that it can act as a good SE [6]. Irrespective of the HT temperatures, $Li_{3-x}Yb_{1-x}Hf_xCl_6$ show the volcano-shaped Li^+ conductivities and the counteracting shape of corresponding activation energies, with the highest Li^+ conductivities of 1.5 and 1.2 mS cm^{-1} and the lowest activation energies of 0.26 and 0.35 eV for the samples prepared at 400 and 500 °C, respectively, at x = 0.40. This type of behavior is observed in

many superionic conductors for which the concentrations of charge carriers of ions or vacancies govern the overall ionic conductivities [47–52]. It has been well documented experimentally and theoretically that creating Na vacancies in Na_3PS_4 and Na_3SbS_4 is highly effective for enhancing Na^+ conductivities up to 10^{-3}–10^{-2} S/cm, which includes the aliovalent substitutions of Na^+ with Ca^{2+} ($Na_{3-2x}Ca_xPS_4$) [49], S^{2-} with Cl^- ($Na_{3-x}PS_{4-x}Cl_x$) [52], and Sb^{5+} with W^{6+} ($Na_{3-x}Sb_{1-x}W_xPS_4$) [50,51]. In particular, our group recently demonstrated a more than two-fold enhancement in the Li^+ conductivity of Li_2ZrCl_6 via aliovalent substitution with M^{3+} ($Li_{2+x}Zr_{1-x}M_xCl_6$, M = Fe, Cr, V) [41]. In this regard, the increased Li^+ conductivity of Li_3YbCl_6 via aliovalent substitution with Hf^{4+} should be largely attributed to the increased charge carrier concentration of Li vacancies [38,41,46]. The decreasing Li^+ conductivities at x > 0.40 would reflect the insufficient amounts of Li^+. In addition, the effect of lattice shrinkage leading to narrowing of the Li^+ channels could not be ignored (Fig. S4) [23,53,54]. The contribution of the structural transitions on Li^+ conductivities, i.e., trigonal to monoclinic for the samples prepared at 400 °C and orthorhombic I to orthorhombic II for the samples prepared at 500 °C, has remained elusive. Trends in the structural evolutions and corresponding Li^+ conductivities with activation energies for Zr^{4+}-substituted Li_3YbCl_6 were also identical to the

results for Hf^{4+}-substituted Li_3YbCl_6. Specifically, the highest Li^+ conductivity of 1.2 mS cm^{-1} with the lowest activation energy of 0.33 eV for Zr^{4+}-substituted Li_3YbCl_6 was obtained for $Li_{2.8}Yb_{0.8}Zr_{0.2}Cl_6$ prepared at $400\ °C$. The similar structural evolution and Li^+ conductivities between Hf^{4+} and Zr^{4+}-substituted Li_3YbCl_6 are not surprising considering their similar ionic radii (Zr^{4+}: 72 pm, Hf^{4+}: 71 pm) (Fig. S5).

Notably, the monoclinic phase for $Li_{3-x}Yb_{1-x}M_xCl_6$ (M = Hf or Zr) that crystallized at $400\ °C$ showed higher Li^+ conductivities and lower activation energies over the entire composition range, as compared to the orthorhombic II phase that crystallized at $500\ °C$. This result implies that the monoclinic structure is more favorable for Li^+ diffusion in $Li_{3-x}Yb_{1-x}M_xCl_6$ (M = Hf or Zr) than in the orthorhombic structure. Importantly, the exclusive contribution of the crystal structure to Li^+ conductivity could be confirmed experimentally. It is well known that the monoclinic structure with ccp anion arrays is more advantageous in terms of ionic conductivity than the hcp-based orthorhombic structure [37,39]. This is rationalized by the 3D channels of ionic migration pathways for the ccp monoclinic structure, which contrasts with the anisotropic ion migration pathways for the hcp structures, such as trigonal and orthorhombic phases [37]. Moreover, the existence of Li^+ ions in tetrahedral sites might lead to more favorable Li^+ diffusion [46,55]. The higher Li^+ conductivity despite the lower HT temperature for the monoclinic $Li_{3-x}Yb_{1-x}Hf_xCl_6$ prepared at $400\ °C$, as compared to the orthorhombic II phase obtained at $500\ °C$, could thus be explained.

Overall, for $Li_{3-x}Yb_{1-x}Hf_xCl_6$ prepared at both 400 and 500 °C, the initial structures of trigonal and orthorhombic I changed to different structures at x = 0.40, that is, monoclinic and orthorhombic II, respectively, and the highest conductivities and the lowest activation energies were obtained. The mean radius of the metal ions for $Li_{2.60}Yb_{0.60}Hf_{0.40}Cl_6$ (80.6 pm) is close to the ionic radius of In^{3+} (80 pm) for Li_3InCl_6 [35] or that for $Li_{2.5}Y_{0.5}Zr_{0.5}Cl_6$ (81 pm) [37]. This explains why the monoclinic or orthorhombic II structures evolve for $Li_{3-x}Yb_{1-x}Hf_xCl_6$. It is noted that the threshold temperatures for the evolution of specific structures vary with composition. $Li_{3-x}Yb_{1-x}Hf_xCl_6$ and $Li_{3-x}Y_{1-x}Zr_xCl_6$ crystallized to the orthorhombic II phase at different temperatures: 400–500 °C and 300–400 °C, respectively, which emphasizes that not only the size of the metal ions but also the HT protocol is a critical factor in the phase transition.

For an in-depth analysis, Rietveld refinement was carried out for the HRXRD patterns of the samples showing the highest Li^+ conductivities, namely $Li_{2.60}Yb_{0.60}Hf_{0.40}Cl_6$ prepared at 400 or 500 °C, and the results are shown in Fig. 4 and Tables S3–S6. For $Li_{2.60}Yb_{0.60}Hf_{0.40}Cl_6$ prepared at 400 °C, the monoclinic and orthorhombic II phases were present in ratios of 70.5% and 29.5%, respectively. From this result, it is expected that the Li^+ conductivity of the pure monoclinic phase would be slightly higher than the measured value (1.5 mS cm^{-1}). Unfortunately, attempts to obtain the pure monoclinic phase of $Li_{2.60}Yb_{0.60}Hf_{0.40}Cl_6$ via HT at lower temperatures have not been successful. The sample prepared at <

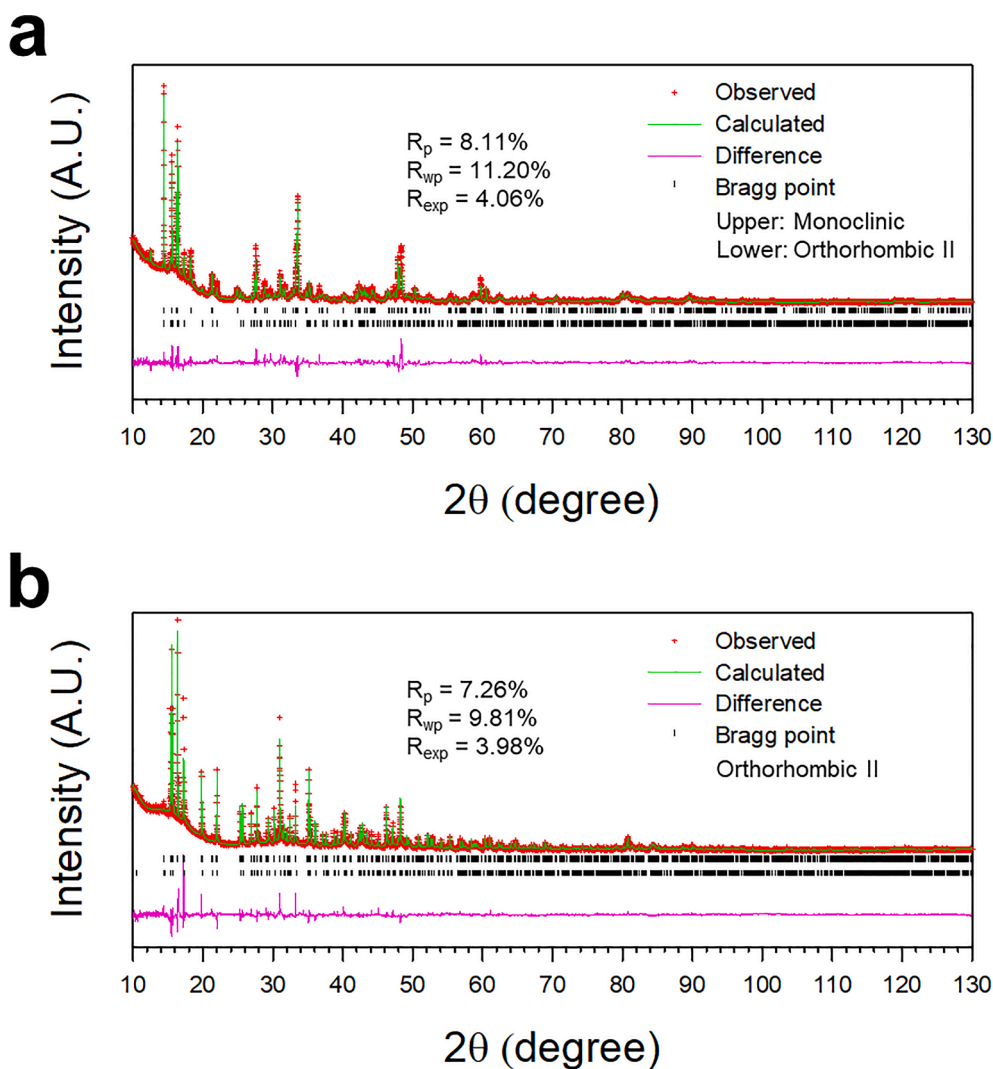**Fig. 4.** Observed and calculated high-resolution synchrotron radiation X-ray Rietveld refinement profiles for $Li_{2.60}Yb_{0.60}Hf_{0.40}Cl_6$ annealed at (a) 400 °C and (b) 500 °C. The Bragg positions in (b) indicate orthorhombic II phases with different lattice parameters. Detailed refinement results are shown in Tables S3–S6.

400 °C also showed the signatures of the orthorhombic II phase and poor crystallinity, inhibiting refinement (Fig. S6). The HRXRD patterns of $Li_{2.60}Yb_{0.60}Hf_{0.40}Cl_6$ prepared at 500 °C were best fitted with two phases belonging to the same space group of orthorhombic II structure with different lattice parameters (Tables S5 and S6). Compositions of the two phases with the different lattice parameters may differ each other. It was reported that a multi-phase region appears during the synthesis of layered $NaMO_2$ (M = Fe, Co) cathode materials via HT or charge–discharge processes [55–57]. In addition, lattice parameters of crystalline SE materials could vary with the extent of annealing [44]. It seems that the separated regions with different phases that formed at lower temperatures (e.g., 400 °C) evolved to the identical orthorhombic II phase but with different lattice parameters at an elevated temperature of 500 °C.

Finally, the compatibility of the optimal-composition Hf^{4+}-substituted Li_3YbCl_6 ($Li_{2.60}Yb_{0.60}Hf_{0.40}Cl_6$) showing the highest Li^+ conductivity (1.5 mS cm^{-1}, prepared at 400 °C) with newly emerging single-NCA88 cathode materials was assessed by cycling half cells in the voltage range of 3.0–4.3 V (vs. Li/Li$^+$) at 0.5C and 30 °C. The deformability of $Li_{2.60}Yb_{0.60}Hf_{0.40}Cl_6$ was confirmed by the flattened surface of the pellet, which was cold-pressed at an applied pressure of 370 MPa (Fig. S7). The cycling performance and corresponding charge–discharge voltage profiles at the 2nd, 150th, 500th, and 1000th cycles are displayed in Fig. 5. The all-solid-state cells showed high discharge capacity and Coulombic efficiency at an initial cycle of 188 mA h g^{-1} and 84.8%, respectively. Impressively, the capacity retention at the 1000th cycle was as high as 83.6%. The attempt to increase the fraction of single-NCA88 in the electrodes from 50 to 70 wt% was offset by the slightly

degraded cycling performance (Fig. S8). This result indicates that the spatial distribution of single-NCA88 particles with 30 wt% $Li_{2.60}Yb_{0.60}Hf_{0.40}Cl_6$ is not perfectly even enough to avoid direct contacts between single-NCA88 particles, which is detrimental to the electrochemo-mechanical degradation of the electrodes due to the repeated volumetric strains upon charge–discharge cycles [58]. Moreover, all-solid-state cells were prepared using $Li_{2.80}Yb_{0.80}Zr_{0.20}Cl_6$ which was prepared at 400 °C and showed the highest ionic conductivity of 1.2 mS cm^{-1} at 30 °C. The cells using $Li_{2.80}Yb_{0.80}Zr_{0.20}Cl_6$ showed the similar electrochemical performances, as compared with the results for using $Li_{2.60}Yb_{0.60}Hf_{0.40}Cl_6$ (Fig. S9). Importantly, the cycling retention for the cells using $Li_{2.80}Yb_{0.80}Zr_{0.20}Cl_6$ was also excellent. Besides, Zr-based materials inevitably include Hf impurities [59]. The similar electrochemical performances of the cells using $Li_{2.80}Yb_{0.80}Zr_{0.20}Cl_6$ and $Li_{2.60}Yb_{0.60}Hf_{0.40}Cl_6$ suggest no need to separate $HfCl_4$ or $ZrCl_4$ from precursor mixtures, which may be an advantageous feature in terms of the manufacturing cost.

3. Conclusions

In summary, the structural evolution and corresponding Li^+ conductivities of Hf^{4+} or Zr^{4+}-substituted Li_3YbCl_6, varied by two different HT temperatures of 400 and 500 °C, were investigated. Unsubstituted Li_3YbCl_6 crystallized differently depending on the HT temperatures: trigonal and orthorhombic I structures resulted when prepared at 400 and 500 °C, respectively, with a slightly higher Li^+ conductivity (0.19 vs. 0.15 mS cm^{-1}) and lower activation energy for the former (0.47 vs. 0.53 eV). Upon aliovalent substitution with Hf^{4+} or Zr^{4+}, the Li^+
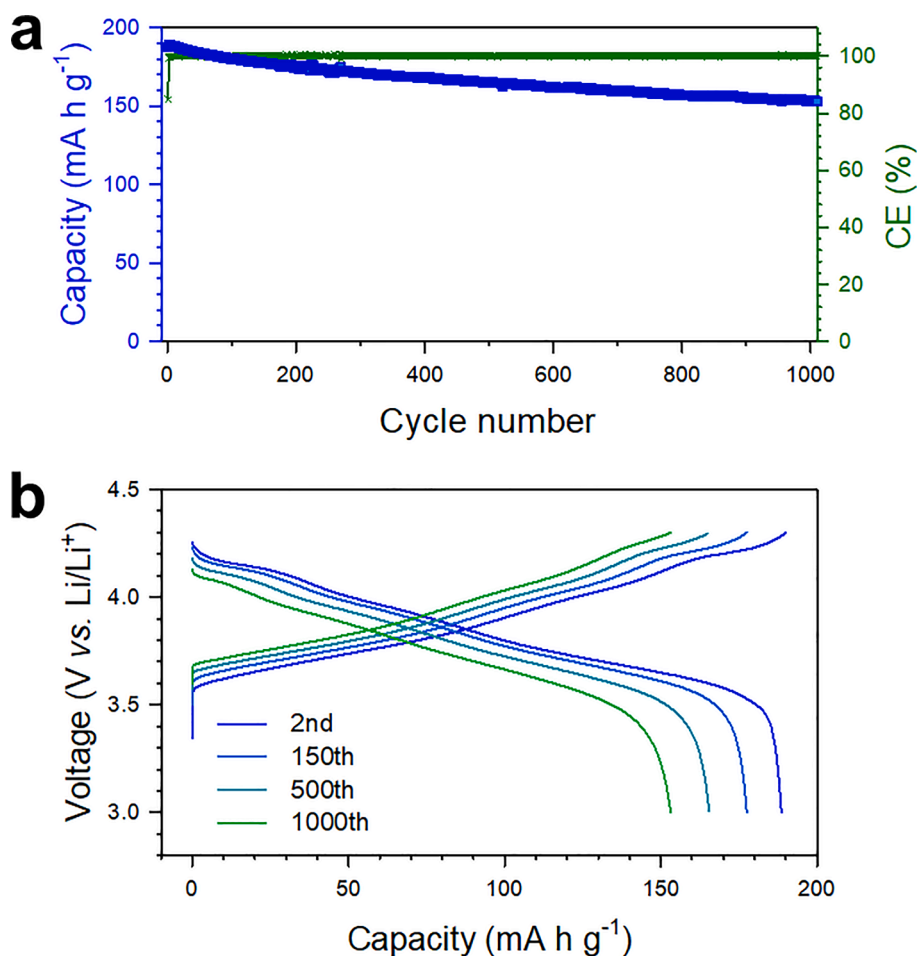

Fig. 5. (a) Cycling performance of single-NCA88 electrodes employing $Li_{2.60}Yb_{0.40}Hf_{0.40}Cl_6$ in single-NCA88/Li-In all-solid-state cells at 0.5C (0.64 mA cm^{-2}) and 30 °C and (b) corresponding charge discharge voltage profiles.

conductivities were boosted to a maximum of 1.5 mS cm^{-1} with the lowest activation energy of 0.26 eV along with drastic phase evolutions: trigonal to monoclinic for HT at 400 °C and orthorhombic I to orthorhombic II for HT at 500 °C. Over the entire ranges, $Li_{3-x}Yb_{1-x}Hf_xCl_6$ exhibited higher Li$^+$ conductivities and lower activation energies when heat-treated at a lower temperature of 400 °C, which unprecedentedly confirmed the exclusive effect of crystal structure on Li$^+$ diffusion in this class of halide SEs, i.e., more favorable in the monoclinic structure than in the orthorhombic structure. Benefitting from the highest Li$^+$ conductivity of 1.5 mS cm^{-1} for the optimal composition of $Li_{2.60}Yb_{0.60}Hf_{0.40}Cl_6$ along with its intrinsic (electro)chemical-oxidation-tolerable property, the single-NCA88 demonstrated a high reversible capacity of 188 mA h g^{-1} and an excellent capacity retention of 83.6% at the 1000th cycle. These results are important in terms of not only practical applicability to all-solid-state technologies but also design principles for new halide superionic conductors.

4. Experimental

4.1. Preparation of materials

All the sample preparation was conducted under Ar atmosphere. Stoichiometric amounts of precursors were mechanically milled at 600 rpm for 10 h in a 50 ml ZrO_2 vial with 15 ea ZrO_2 balls ($\phi = 10$ mm) using Pulverisette 7 PL (Fritsch GmbH). For the preparation of $Li_{3-x}Yb_{1-x}Hf_xCl_6$, LiCl (99.99%, Sigma Aldrich), YbCl$_3$ (99.9%, Alfa Aesar), and HfCl$_4$ (99%, Alfa Aesar) were used. For the preparation of $Li_{3-x}Yb_{1-x}Zr_xCl_6$, LiCl, YbCl$_3$, and ZrCl$_4$ (99.99%, Sigma Aldrich) were used. For the preparation of $Li_{3-x}Y_{1-x}Zr_xCl_6$, LiCl, YCl$_3$ (99.99%, Sigma Aldrich), and ZrCl$_4$ were used. Ball-milled powder samples were sealed in a quartz ampoule under vacuum and then heat-treated at target temperatures for 6 h with a heating rate of 5 °C min^{-1} and natural cooling at room temperature. $Li_6PS_5Cl_{0.5}Br_{0.5}$ was prepared by mechanical milling and subsequently HT. A stoichiometric amount of Li$_2$S (99.9%, Alfa Aesar), P$_2$S$_5$ (99%, Sigma Aldrich), LiCl, and LiBr (99.99%, Sigma Aldrich) was milled with the condition as the same as for halide SEs, which was followed by HT at 550 °C at 12 h with Ar flow.

4.2. Materials characterization

Powder XRD patterns (Lab scale) were collected using a Rigaku MiniFlex600 diffractometer with Cu K$_\alpha$ radiation ($\lambda = 1.5406$ Å). XRD cells containing hermetically-sealed SE samples with a Beryllium window were mounted on an XRD diffractometer and measured at 40 kV and 15 mA. High-resolution synchrotron radiation X-ray data were acquired at a 9B beamline in the Pohang Accelerator Laboratory (PAL, South Korea) using monochromatic X-ray ($\lambda = 1.5220$ Å). The quantitative structural information was obtained by Rietveld refinement method using the FullProf Suite software package. SEM images were obtained using AURIGA (Zeiss). To avoid any air exposure of the samples, an air-tight transfer box, DME 2830 (SEMILAB), was used.

4.3. Electrochemical characterization

Li$^+$ conductivities were measured by AC impedance method using Li$^+$-blocking Ti/SE/Ti symmetric cells with 6 mm diameter. The cold-pressed pellets were prepared under an applied pressure of 370 MPa. The EIS data were recorded with an amplitude of 100 mV and a frequency range from 10 mHz to 7 MHz using a VMP3 (Bio-Logic). For the all-solid-state half-cells, Li-In counter and reference electrodes were used. The Li-In electrodes with a nominal composition of $Li_{0.5}$In were prepared by ball-milling of In (Aldrich, 99%), Li (FMC Lithium Corp.), and $Li_6PS_5Cl_{0.5}Br_{0.5}$ powders in a weight ratio of 8:2. $Li_6PS_5Cl_{0.5}Br_{0.5}$ powders of 150 mg were pelletized under 100 MPa to form SE layers. Composite working electrodes were prepared from a mixture of single-NCA88, $Li_{2.60}Yb_{0.60}Hf_{0.40}Cl_6$ or $Li_{2.80}Yb_{0.80}Zr_{0.20}Cl_6$ prepared at

400 °C for 6 h, and super C65 powders in a weight ratio of 70:30:3 or 50:50:3. Then, the working and Li-In counter electrodes were put on each side of the SE layers. Finally, the whole assemblies were pressed at 370 MPa at room temperature. The all-solid-state cells were tested under an external pressure of ∼ 70 MPa at 30 °C.

Declaration of Competing Interest

The authors declare that they have no known competing financial interests or personal relationships that could have appeared to influence the work reported in this paper.

Appendix A. Supplementary data

Supplementary data to this article can be found online at https://doi.org/10.1016/j.cej.2021.130630.

References

[1] W. Li, E.M. Erickson, A. Manthiram, High-nickel layered oxide cathodes for lithium-based automotive batteries, Nat. Energy 5 (2020) 26–34, https://doi.org/10.1038/s41560-019-0513-0.

[2] B. Dunn, H. Kamath, J.-M. Tarascon, Electrical energy storage for the grid: a battery of choices, Sci. 334 (6058) (2011) 928–935, https://doi.org/10.1126/science.1212741.

[3] J. Janek, W.G. Zeier, A solid future for battery development, Nat. Energy 1 (2016) 1–4, https://doi.org/10.1038/nenergy.2016.141.

[4] A. Hayashi, K. Noi, A. Sakuda, M. Tatsumisago, Superionic glass-ceramic electrolytes for room-temperature rechargeable sodium batteries, Nat. Commun. 3 (2012) 1–5, https://doi.org/10.1038/ncomms1843.

[5] Y. Kato, S. Hori, T. Saito, K. Suzuki, M. Hirayama, A. Mitsui, M. Yonemura, H. Iba, R. Kanno, High-power all-solid-state batteries using sulfide superionic conductors, Nat. Energy 1 (2016) 1–7, https://doi.org/10.1038/nenergy.2016.30.

[6] K.H. Park, Q. Bai, D.H. Kim, D.Y. Oh, Y. Zhu, Y. Mo, Y.S. Jung, Design strategies, practical considerations, and new solution processes of sulfide solid electrolytes for all-solid-state batteries, Adv. Energy Mater. 8 (2018) 1800035, https://doi.org/10.1002/aenm.201800035.

[7] Z. Zhang, Y. Shao, B. Lotsch, Y.-S. Hu, H. Li, J. Janek, L.F. Nazar, C.-W. Nan, J. Maier, M. Armand, L. Chen, New horizons for inorganic solid state ion conductors, Energy Environ. Sci. 11 (2018) 1945–1976, https://doi.org/10.1039/c8ee01053f.

[8] Q. Zhang, D. Cao, Y. Ma, A. Natan, P. Aurora, H. Zhu, Sulfide-based solid-state electrolytes: synthesis, stability, and potential for all-solid-state batteries, Adv. Mater. 31 (2019) 1901131, https://doi.org/10.1002/adma.201901131.

[9] R. Chen, Q. Li, X. Yu, L. Chen, H. Li, Approaching practically accessible solid-state batteries: stability issues related to solid electrolytes and interfaces, Chem. Rev. 120 (2020) 6820–6877, https://doi.org/10.1021/acs.chemrev.9b00268.

[10] X. Han, Y. Gong, K.K. Fu, X. He, G.T. Hitz, J. Dai, A. Pearse, B. Liu, H. Wang, G. Rubloff, Y. Mo, V. Thangadurai, E.D. Wachsman, L. Hu, Negating interfacial impedance in garnet-based solid-state Li metal batteries, Nat. Mater. 16 (2017) 572–579, https://doi.org/10.1038/nmat4821.

[11] R. Murugan, V. Thangadurai, W. Weppner, Fast lithium ion conduction in garnet-type Li$_7$La$_3$Zr$_2$O$_{12}$, Angew. Chem. Int. Ed. 46 (2007) 7778–7781, https://doi.org/10.1002/anie.200701144.

[12] M.J. Wang, R. Choudhury, J. Sakamoto, Characterizing the Li-solid-electrolyte interface dynamics as a function of stack pressure and current density, Joule 3 (2019) 2165–2178, https://doi.org/10.1016/j.joule.2019.06.017.

[13] S. Xiong, X. He, A. Han, Z. Liu, Z. Ren, B. McElhenny, A.M. Nolan, S. Chen, Y. Mo, H. Chen, Computation-guided design of LiTaSiO$_5$, a new lithium ionic conductor with sphene structure, Adv. Energy Mater. 9 (2019) https://doi.org/10.1002/aenm.201803821.

[14] F. Han, J. Yue, C. Chen, N. Zhao, X. Fan, Z. Ma, T. Gao, F. Wang, X. Guo, C. Wang, Interphase engineering enabled all-ceramic lithium battery, Joule 2 (2018) 497–508, https://doi.org/10.1016/j.joule.2018.02.007.

[15] R. Pfenninger, M. Struzik, I. Garbayo, E. Stilp, J.L.M. Rupp, A low ride on processing temperature for fast lithium conduction in garnet solid-state battery

films, Nat. Energy 4 (2019) 475–483, https://doi.org/10.1038/s41560-019-0384-4.

[16] K.H. Kim, Y. Iriyama, K. Yamamoto, S. Kumazaki, T. Asaka, K. Tanabe, C.A. Fisher, T. Hirayama, R. Murugan, Z. Ogumi, Characterization of the interface between LiCoO₂ and Li₇La₃Zr₂O₁₂ in an all-solid-state rechargeable lithium battery, J. Power Sources 196 (2011) 764–767, https://doi.org/10.1016/j.jpowsour.2010.07.073.

[17] M. Kotobuki, H. Munakata, K. Kanamura, Y. Sato, T. Yoshida, Compatibility of Li₇La₃Zr₂O₁₂ solid electrolyte to all-solid-state battery using Li metal anode, J. Electrochem. Soc. 157 (2010) A1076, https://doi.org/10.1149/1.3474232.

[18] J. Wan, J. Xie, D.G. Mackanic, W. Burke, Z. Bao, Y. Cui, Status, promises, and challenges of nanocomposite solid-state electrolytes for safe and high performance lithium batteries, Mater. Today Nano 4 (2018) 1, https://doi.org/10.1016/j.mtnano.2018.12.003.

[19] Q. Zhou, J. Ma, S. Dong, X. Li, G. Cui, Intermolecular chemistry in solid polymer electrolytes for high-energy-density lithium batteries, Adv. Mater. 31 (2019) 1902029, https://doi.org/10.1002/adma.201902029.

[20] S. Tang, W. Guo, Y. Fu, Advances in composite polymer electrolytes for lithium batteries and beyond, Adv. Energy Mater. 11 (2020) 2000802, https://doi.org/10.1002/aenm.202000802.

[21] H.J. Deiseroth, S.T. Kong, H. Eckert, J. Vannahme, C. Reiner, T. Zaiß, M. Schlosser, Li₆PS₅X: a class of crystalline Li-rich solids with an unusually high Li⁺ mobility, Angew. Chem. Int. Ed. 120 (2008) 767–770, https://doi.org/10.1002/ange.200703900.

[22] N.J.J. de Klerk, T. Roslon, M. Wagemaker, Diffusion mechanism of Li argyrodite solid electrolytes for Li-Ion batteries and prediction of optimized halogen doping: the effect of Li vacancies, halogens, and halogen disorder, Chem. Mater. 28 (2016) 7955–7963, https://doi.org/10.1021/acs.chemmater.6b03630.

[23] H. Kwak, K.H. Park, D. Han, K.-W. Nam, H. Kim, Y.S. Jung, Li⁺ conduction in air-stable Sb-substituted Li₄SnS₄ for all-solid-state Li-Ion batteries, J. Power Sources 446 (2020) 227338, https://doi.org/10.1016/j.jpowsour.2019.227338.

[24] M.A. Kraft, S.P. Culver, M. Calderon, F. Böcher, T. Krauskopf, A. Senyshyn, C. Dietrich, A. Zevalkink, J. Janek, W.G. Zeier, Influence of lattice polarizability on the ionic conductivity in the lithium superionic argyrodites Li₆PS₅X (X= Cl, Br, I), J. Am. Chem. Soc. 139 (2017) 10909–10918, https://doi.org/10.1021/jacs.7b06327.

[25] P. Wang, H. Liu, S. Patel, X. Feng, P.-H. Chien, Y. Wang, Y.-Y. Hu, Fast ion conduction and its origin in Li₆₋ₓPS₅₋ₓBr₁₊ₓ, Chem. Mater. 32 (2020) 3833–3840, https://doi.org/10.1021/acs.chemmater.9b05331.

[26] L. Zhou, A. Assoud, Q. Zhang, X. Wu, L.F. Nazar, New family of argyrodite thioantimonate lithium superionic Conductors, J. Am. Chem. Soc. 141 (2019) 19002–19013, https://doi.org/10.1021/jacs.9b08357.

[27] K.H. Park, D.Y. Oh, Y.E. Choi, Y.J. Nam, L. Han, J.-Y. Kim, H. Xin, F. Lin, S.M. Oh, Y.S. Jung, Solution-processable glass LiI-Li₄SnS₄ superionic conductors for all-solid-state Li-ion batteries, Adv. Mater. 28 (2016) 1874–1883, https://doi.org/10.1002/adma.201505008.

[28] W.D. Richards, L.J. Miara, Y. Wang, J.C. Kim, G. Ceder, Interface stability in solid-state batteries, Chem. Mater. 28 (2016) 266–273, https://doi.org/10.1021/acs.chemmater.5b04082.

[29] S.H. Jung, K. Oh, Y.J. Nam, D.Y. Oh, P. Bruener, K. Kang, Y.S. Jung, Li₃BO₃-Li₂CO₃: rationally designed buffering phase for sulfide all solid-state Li-ion batteries, Chem. Mater. 30 (2018) 8190–8200, https://doi.org/10.1021/acs.chemmater.8b03321.

[30] S.H. Jung, U.H. Kim, J.H. Kim, S. Jun, C.S. Yoon, Y.S. Jung, Y.K. Sun, Ni-Rich layered cathode materials with electrochemo-mechanically compliant microstructures for all-solid-state Li batteries, Adv. Energy Mater. 10 (2020) 1903360, https://doi.org/10.1002/aenm.201903360.

[31] F. Walther, R. Koerver, T. Fuchs, S. Ohno, J. Sann, M. Rohnke, W.G. Zeier, J. Janek, Visualization of the interfacial decomposition of composite cathodes in argyrodite based all-solid-state batteries using time-of-flight secondary ion mass spectrometry, Chem. Mater. 31 (2019) 3745–3755, https://doi.org/10.1021/acs.chemmater.9b00770.

[32] L. Duchene, A. Remhof, H. Hagemann, C. Battaglia, Status and prospects of hydroborate electrolytes for all-solid-state batteries, Energy Storage Mater. 25 (2020) 782–794, https://doi.org/10.1016/j.ensm.2019.08.032.

[33] S. Kim, H. Oguchi, N. Toyama, T. Sato, S. Takagi, T. Otomo, D. Arunkumar, N. Kuwata, J. Kawamura, S.-I. Orimo, A complex hydride lithium superionic conductor for high-energy-density all-solid-state lithium metal batteries, Nat. Commun. 10 (2019) 1081, https://doi.org/10.1038/s41467-019-09061-9.

[34] T. Asano, A. Sakai, S. Ouchi, M. Sakaida, A. Miyazaki, S. Hasegawa, Solid halide electrolytes with high lithium-ion conductivity for application in 4 V Class bulk-type all-solid-state batteries, Adv. Mater. 30 (2018) 1803075, https://doi.org/10.1002/adma.201803075.

[35] X. Li, J. Liang, J. Luo, M.N. Banis, C. Wang, W. Li, S. Deng, C. Yu, F. Zhao, X. Sun, Air-stable Li₃InCl₆ electrolyte with high voltage compatibility for all-solid-state batteries, Energy Environ. Sci. 12 (2019) 2665–2671, https://doi.org/10.1039/C9EE02311A.

[36] S. Wang, Q. Bai, A.M. Nolan, Y. Liu, S. Gong, Q. Sun, Y. Mo, Lithium chlorides and bromides as promising solid-state chemistries for fast ion conductors with good electrochemical stability, Angew. Chem. Int. Ed. 58 (2019) 8039–8043, https://doi.org/10.1002/anie.201901938.

[37] D. Park, H. Park, Y. Lee, S.-O. Kim, H.-G. Jung, K.Y. Chung, J.H. Shim, S. Yu, Theoretical design of lithium chloride superionic conductors for all-solid-state

[38] J. Liang, X. Li, S. Wang, K.R. Adair, W. Li, Y. Zhao, C. Wang, Y. Hu, L. Zhang, Y. Mo, X. Sun, Site-occupation-tuned superionic LiₓScCl₃₊ₓ halide solid electrolytes for all-solid-state batteries, J. Am. Chem. Soc. 142 (2020) 7012–7022, https://doi.org/10.1021/jacs.0c00134.

[39] X. Li, J. Liang, K.R. Adair, J. Li, W. Li, F. Zhao, Y. Hu, T.-K. Sham, L. Zhang, S. Zhao, X. Sun, Origin of superionic Li₃Y₁₋ₓInₓCl₆ halide solid-electrolytes with high humidity tolerance, Nano Lett. 20 (2020) 4384–4392, https://doi.org/10.1021/acs.nanolett.0c01156.

[40] L. Nazar, L. Zhou, C.Y. Kwok, A. Shyamsunder, Q. Zhang, X. Wu, A new halospinel superionic conductor for high-voltage all solid state lithium batteries, Energy Environ. Sci. 13 (2020) 2056–2063, https://doi.org/10.1039/D0EE01017K.

[41] H. Kwak, D. Han, J. Lyoo, J. Park, S.H. Jung, Y. Han, G. Kwon, H. Kim, S.-T. Hong, K.-W. Nam, Y.S. Jung, New cost-effective halide solid electrolytes for all-solid-state batteries: mechanochemically prepared Fe³⁺-substituted Li₂ZrCl₆, Adv. Energy Mater. (2021) 2003190, https://doi.org/10.1002/aenm.202003190.

[42] H. Kwak, J. Lyoo, J. Park, Y. Han, R. Asakura, A. Remhof, C. Battaglia, H. Kim, S.-T. Hong, Y.S. Jung, Na₂ZrCl₆ enabling highly stable 3 V all-solid-state Na-ion batteries, Energy Storage Mater. 37 (2021) 47–54, https://doi.org/10.1016/j.ensm.2021.01.026.

[43] A. Bohnsack, F. Stenzel, A. Zajonc, G. Balzer, M. Wickleder, G. Meyer, Ternary halides of the A₃MX₆ type. Part 6. Ternary chlorides of the rare-earth elements with lithium, Li₃LnCl₆ (Ln: Tb-Lu, Y, Sc): Synthesis, Crystal Structures, and Ionic Motion, J. Cheminf. 623 (1997) 1067–1073, https://doi.org/10.1002/zaac.19976230710.

[44] R. Schlem, S. Muy, N. Prinz, A. Banik, Y. Shao-Horn, M. Zobel, W.G. Zeier, Mechanochemical synthesis: a tool to tune cation site disorder and ionic transport properties of Li₃MCl₆ (M= Y, Er) superionic conductors, Adv. Energy Mater. 10 (2020) 1903719, https://doi.org/10.1002/aenm.201903719.

[45] Y. Liu, S. Wang, A.M. Nolan, C. Ling, Y. Mo, Tailoring the cation lattice for chloride lithium-ion conductors, Adv. Energy Mater. 10 (2020) 2002356, https://doi.org/10.1002/aenm.202002356.

[46] Z. Liu, S. Ma, J. Liu, S. Xiong, Y. Ma, H. Chen, High ionic conductivity achieved in Li₃Y(Br 3Cl3) mixed halide solid electrolyte via promoted diffusion pathways and enhanced grain boundary, ACS Energy Lett. 6 (2020) 298–304, https://doi.org/10.1021/acsenergylett.0c01690.

[47] A.R. West, Basic Solid State Chemistry, John Wiley & Sons Ltd., England, 1999.

[48] J.W. Heo, A. Banerjee, K.H. Park, Y.S. Jung, S.-T. Hong, Na-ion solid electrolytes Na₄₋ₓSn₁₋ₓSbₓS₄ (0.02 < x < 0.33) for all-solid-state Na-ion batteries, Adv. Energy Mater. 8 (2018) 1702716, https://doi.org/10.1002/aenm.201702716.

[49] C.K. Moon, H.-J. Lee, K.H. Park, H. Kwak, J.W. Heo, K. Choi, H. Yang, M.-S. Kim, S.-T. Hong, J.H. Lee, Y.S. Jung, Vacancy-driven Na⁺ superionic conduction in new Ca-doped Na₃PS₄ for all-solid-state Na-ion batteries, ACS Energy Lett. 3 (2018) 2504–2512, https://doi.org/10.1021/acsenergylett.8b01479.

[50] R. Jalem, A. Hayashi, F. Tsuji, A. Sakuda, Y. Tateyama, First-principles calculation study of Na⁺ superionic conduction mechanism in W-and Mo-doped Na₃SbS₄ solid electrolytes, Chem. Mater. 32 (2020) 8373–8381, https://doi.org/10.1021/acs.chemmater.0c02318.

[51] A. Hayashi, N. Masuzawa, S. Yubuchi, F. Tsuji, C. Hotehama, A. Sakuda, M. Tatsumisago, A sodium-ion sulfide solid electrolyte with unprecedented conductivity at room temperature, Nat. Commun. 10 (2019) 1–6, https://doi.org/10.1038/s41467-019-13178-2.

[52] I.-H. Chu, C.S. Kompella, H. Nguyen, Z. Zhu, S. Hy, Z. Deng, Y.S. Meng, S.P. Ong, Room-temperature all-solid-state rechargeable sodium-ion batteries with a Cl-doped Na₃PS₄ superionic conductor, Sci. Rep. 6 (2016) 33733, https://doi.org/10.1038/srep33733.

[53] Z. Yu, S.L. Shang, J.H. Seo, D. Wang, X. Luo, Q. Huang, S. Chen, J. Lu, X. Li, Z.K. Liu, D. Wang, Exceptionally high ionic conductivity in Na₃P₀.₆₂As₀.₃₈S₄ with improved moisture stability for solid-state sodium-ion batteries, Adv. Mater. 29 (2017) 1605561, https://doi.org/10.1002/adma.201605561.

[54] K. Nam, H. Chun, J. Hwang, B. Han, First-principles design of highly functional sulfide electrolyte of Li₁₀₋ₓSnP₂S₁₂₋ₓClₓ for all solid-state Li-ion battery applications, ACS Sustainable Chem. Eng. 8 (8) (2020) 3321–3327, https://doi.org/10.1021/acssuschemeng.9b07166.

[55] R. Schlem, A. Banik, S. Ohno, E. Suard, W.G. Zeier, Insights into the lithium sub-structure of superionic conductors Li₃YCl₆ and Li₃YBr 6, Chem. Mater. 33 (2021) 327–337, https://doi.org/10.1021/acs.chemmater.0c04352.

[56] D. Susanto, M.K. Cho, G. Ali, J.-Y. Kim, H.J. Chang, H.-S. Kim, K.-W. Nam, K.Y. Chung, Anionic redox activity as a key factor in the performance degradation of NaFeO₂ cathodes for sodium ion batteries, Chem. Mater. 31 (2019) 3644–3651, https://doi.org/10.1021/acs.chemmater.9b00149.

[57] Y. Lei, X. Li, L. Liu, G. Ceder, Synthesis and stoichiometry of different layered sodium cobalt oxides, Chem. Mater. 26 (2014) 5288–5296, https://doi.org/10.1021/cm5021788.

[58] Y. Han, S.H. Jung, H. Kwak, S. Jun, H.H. Kwak, J.H. Lee, S.T. Hong, Y.S. Jung, Single-or poly-crystalline Ni-rich layered cathode, sulfide or halide solid electrolyte: which will be the winners for all-solid-state batteries? Adv. Energy Mater. (2021) 2100126, https://doi.org/10.1002/aenm.202100126.

[59] L. Xu, Y. Xiao, A. van Sandwijk, Q. Xu, Y. Yang, Separation of zirconium and hafnium: a review, Energy Mater. 2014 (2014) 451–457, https://doi.org/10.1007/978-3-319-48765-6_53.